Current Drive and Heating in a D-He^3 FRC Reactor, Relaxation in a Flux Core Spheromak and Oscillating Field Current Drive.

R. Farengo, H. E. Ferrari, P. L. García Martínez
Centro Atómico Bariloche e Instituto Balseiro, 8400 Bariloche, RN, Argentina
E-mail:farengo@cab.cnea.gov.ar

R. A. Clemente, M. Gilli
Instituto de Fisica Gleb Wataghin, UNICAMP, 13083-970 Campinas, SP, Brazil

Current drive and heating in a D-He^3 FRC reactor

Field Reversed Configurations (FRC) could operate with advanced fuel cycles due to their high β value. We studied the use of neutral beams (NBI) [1] and fusion protons and α-particles [2] to heat the plasma and sustain the current in a *D-He*^{3} FRC reactor. The plasma parameters employed are similar to those proposed in the ARTEMIS conceptual reactor design [3] (T_e=T_i=87.5 keV, B_{ext}=6.7 T, a=1.12 m, L=17 m, n_D/n_e=0.5, n_{He}/n_e =0.25).

A Monte Carlo code previously employed to study NBI in FRCs and Spheromaks [4,5] was used to study the interaction of the NB and the fusion born protons and α-particles with the plasma. The code follows the exact particle orbits (no gyro-averaging) and includes particle drag and pitch angle scattering. An ionization package is included in the NBI studies to calculate the position and velocity of the neutrals when they ionize. Isotropic proton and α-particle sources distributed inside the FRC according to the fusion reaction rate are considered when studying the interaction of these particles with the plasma. The equilibria employed in both cases were obtained by numerically solving the Grad-Shafranov equation with a pressure that includes linear and cuadratic terms in the poloidal magnetic flux. The shape of the equilibrium, "peaked" or "hollow", can be adjusted by changing the coefficient of the cuadratic (in the flux) term in the pressure.

The NBI studies show that the beam current predicted in [3] (8 MA) can not be obtained with the proposed neutral energy (1 MeV) and current (5 A). A simple theoretical calculation that includes a velocity dependent particle drag and assumes perfectly circular orbits gives a total current of only 1.2 MA. The current calculated with the code was 0.32 MA for a peaked equilibrium (E1 in table 1 below) and even lower for a hollow equilibrium (E2). There are three reasons that explain why the current calculated with the code is lower than the theoretical calculation. The first one is that a fraction of the ionized particles, approximately 18% for peaked and 62% for hollow equilibria, is lost through the ends of the configuration before becoming thermalized and hence their contribution to the current is smaller than assumed in the theoretical calculation. These losses could be reduced adding magnetic mirrors but the resulting magnetic field structure has to be compatible with the direct energy converters included in the ARTEMIS design. The second one is that due to the particular magnetic field structure of FRCs a fraction of the inyected neutral particles, those ionized close to the separatrix, end up rotating around the FRC in the counter current sense ("negative" particles). The third one is that, due to the low beam energy, most "positive" particles have orbits with large radial oscillations while circular orbits were assumed in the theoretical calculation.

Fig. 1 shows the initial orbits of particles ionized at different locations (collisions not included). In Fig. 1*a* the particles rotate in the current sense ("positive") while in Fig. 1*b* they rotate in the "negative" sense. In both figures, *1* and *2* indicate the position where the particles where ionized and *1'* and *2'* the final position, after the same amount of time. It is clear that positive particles rotate faster than negative ones. Fig. 2 shows the beam current profile for the E1 equilibrium. The beam was inyected at the midplane with impact parameter equal to the null radius, the axial dispersion is due to collisions.

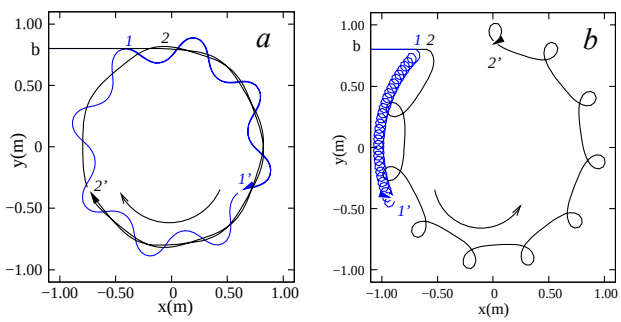

Fig. 1. Orbits of ions ionized at different locations

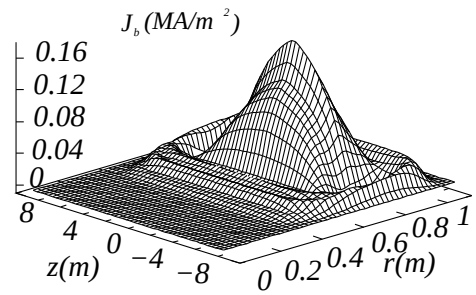

Fig. 2. Beam current profile

The protons (14.6 MeV) and α-particles (3.7 MeV) produced in the *D-He*^{3} fusion reactions can contribute to heat the plasma and sustain the current. Three equilibria were analized, all with the same basic parameters indicated above and different magnetic field and presurre profiles. Different quantities that characterize these equilibria are shown in table 1:

Table 1. Relevant quantities for the different equilibria analyzed

	n_a (10^{20} m^{-3})	N_e ($\times 10^{22}$)	P_p (MW)	P_α (MW)	E_t (MJ)	β
E1	3.2	2.2	336.5	83.8	823.5	0.44
E2	5.5	3.8	766.8	190.9	1427	0.75
E3	3.1	2.15	330.1	82.2	792.9	0.42

where n_a is the average electron density, N_e is the total number of electrons, P_p is the total proton power generated, P_α is the total α-particle power generated, E_t is the total thermal energy of the plasma and β is calculated with the external magnetic field.

An analysis of the proton orbits shows that there are more protons rotating in the current sense ("positive") and that the average azimuthal velocity of these protons is higher than the velocity of those rotating in the opposite sense. In addition, negative current particles tend to be lost much faster than positive ones due to collisions. These two features explain why isotropic proton sources distributed inside the FRC can generate a net current.

The results obtained for the different equilibria are summarized in table 2. I_p and I_α are the proton and α-particle currents, P_{pe} and P_{pi} are the power deposited by the protons on the electrons and ions and $P_{\alpha i}$ and $P_{\alpha e}$ the same for the α-particles. The last column in the table (τ_E) indicates the global energy confinement time that would be needed to sustain the plasma temperature. The proton current can reach the values proposed in [3] but the fraction of the proton power deposited in the plasma is small. This fraction depends strongly on the equilibrium profiles, being 46.6% for E3 and only 16% for E2. This shows that the

equilibrium with the highest fusion power has the poorest proton confinement. Fig. 3 shows the proton current profile and Fig. 4 the profile of the total power deposited by the protons.

Table 2. Current and deposited power

	I_p (MA)	I_α (MA)	$P_{p,e}$ (MW)	$P_{p,i}$ (MW)	$P_{\alpha,e}$ (MW)	$P_{\alpha,i}$ (MW)	τ_E(s)
E1	39.4	1.65	110.8	7.2	16.2	54.8	4.35
E2	34.8	2.9	92.9	2.9	14.9	43.4	9.26
E3	46.6	1.8	141.8	12.1	12.7	41.6	3.80

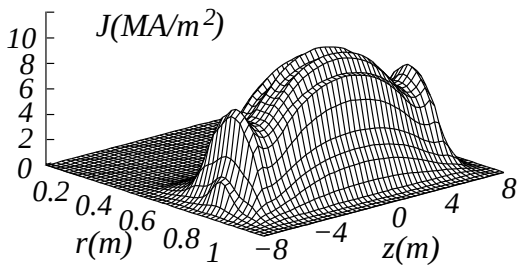

Fig. 3. Proton currrent profile

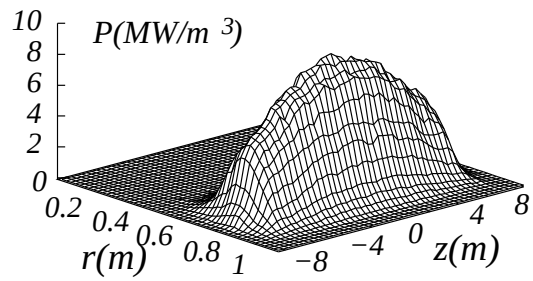

Fig. 4. Deposited proton power

Since the power deposited by the protons is a small fraction of the total generated power it is important to investigate methods to improve proton confinement. We already mentioned the possibility of adding magnetic mirrors to reduce axial losses. We also investigated the effect that a toroidal field would have on the confinement. The self-generation of weak toroidal fields has been observed in experiments where the FRC is formed/sustained by rotating magnetic fields (RMF). Here we investigate the simpler case of an externally produced ("vacuum") toroidal field. The toroidal field is assumed to increase linearly from r=0 to r=0.1 m and decrease like 1/r at larger values of r. The results are presented in Fig. 5, which shows plots of the proton current and deposited power as a function of $B_\theta(r=R)/B_{ext}$, where R is the null radius. It is surprising that both the current and the deposited power decrease sharply at low toroidal field. An analysis of particle losses indicates that for low values of the toroidal field the losses through the ends increase with the toroidal field and the average life time of the particles inside the FRC decreases. When the toroidal field increases beyond the value corresponding to the minimum of P (Fig. 5) radial losses decrease and the average life time of the particles increases.

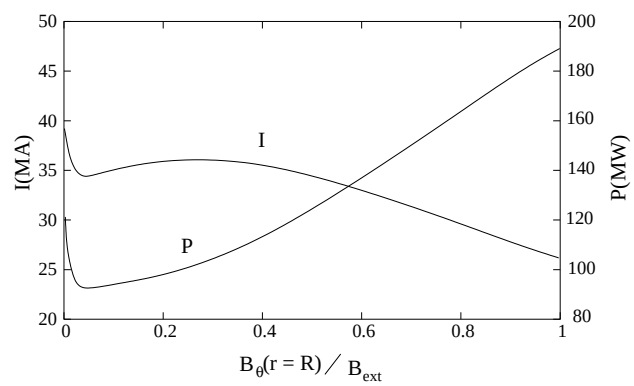

Fig. 5. Proton current and deposited power as a function of the external toroidal field

Relaxation in a flux core spheromak

The spontaneous formation of a Flux-Core Spheromak (FCS) from an unstable screw-pinch was studied using 3-D numerical simulations. The resistive, isothermal MHD equations were solved using the Versatile Advection Code (VAC) [6] which includes a shock-capturing

scheme based in a Roe-type Riemann solver and a Woodward limiter. The divergence-free condition ($\nabla\cdot\mathbf{B}=0$) is maintained using the projection method. To simplify the physics we do not advance the density. This corresponds to a constant pressure computation, usually referred to as the zero-β (or zero-pressure) approximation, widely used when modelling low-β plasmas. The FCS is formed inside a cylindrical flux conserver of radius a with electrodes of radius r_e ($r_e<a$) at both ends.

A uniform cartesian grid is used, with $N_x\times N_y\times N_z=100\times100\times75$. The cylindrical flux conserver is constructed using appropriate values at ghost cells, i.e. knowing the solution inside the flux conserver ($r<a$) we set the values of external grid points ($r>a$) in such a way that the boundary conditions are satisfied (at $r=a$), up to the interpolation error. The perfectly conducting wall conditions employed are: $\mathbf{B}\cdot\hat{n}=0$ and $\mathbf{J}\times\hat{n}=0$. At the electrodes ($r<r_e$, $z=0$ and $r<r_e$, $z=h$), periodic boundary conditions are applied. The initial condition is a force-free screw-pinch, obtained by solving the equation $\nabla\times\mathbf{B}(r)=\lambda(r)\mathbf{B}(r)$ with a *tanh* λ profile that goes smoothly from λ_0 at the electrode $(r<r_e)$ to zero outside $(r_e<r<a)$.

The simulation presented here has normalized cylinder radius and height $a=1$ and $h=1.5$ respectively, and the electrode size is $r_e=0.35$. With this geometry the first eigenfunction of the Taylor state is $\lambda_{\mathrm{Taylor}}=4.3667$. The resistivity is set to $\eta=10^{-4}$. Following Izzo and Jarboe [7], the resistive time scale is $\tau_r=1/\eta\lambda^2\sim500$. The Alfven time scale is taken to be $\tau_A=R\sqrt{\rho}/B_0=1$, since $\rho=1$, and $B_0=B_z(r=0,t=0)=1$; in the following all times are in units of τ_A. With these parameters the Lundquist number of the simulation is $S=\tau_r/\tau_A\sim500$.

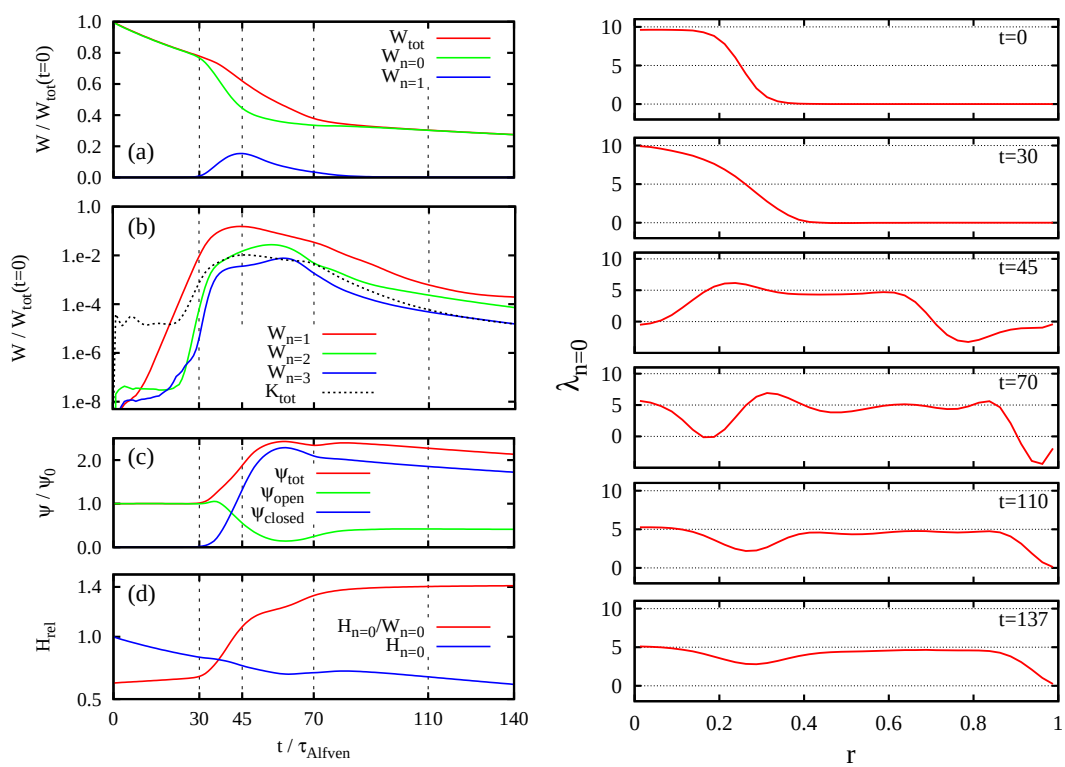

Fig. 6. Rigth:Evolution of the magnetic energy (different modes), kinetic energy, poloidal flux and relative helicity. Left: Profiles of λ at different times

The formation of the FCS can be divided in five phases. Fig. 6 shows, on the left, the evolution of the total magnetic energy (W_{tot}), the kinetic energy (K_{tot}), the energy of the different modes (W_n), the poloidal flux (ψ), the relative helicity of the n=0 mode ($H_{n=0}$) and the ratio $H_{n=0}/W_{n=0}$. The rigth panel shows plots of $\lambda=\mathbf{J}.\mathbf{B}/B^2$ at the transition times between different phases, which are indicated with vertical dotted lines on the left.

In the first phase (t=0 to t=30), the n=1 mode grows rapidly (exponentially) and higher order modes begin to appear. The second phase (t=30 to t=45) shows the saturation of the n=1 mode and the rapid growth of higher order modes. A small amount of kinetic energy also appears. In the third phase (t=45 to t~70) the n=1 energy decreases while higher order modes continue to grow. The fourth phase is the reconnection, which occurs around t=70 and produces the first closed flux tube of the spheromak. The final phase (t>70) involves the generation of the closed flux surfaces of the FCS. After the reconnection all the modes decay and axysimmetry is slowly recovered.

The plots of λ show that initially all the current is concentrated in the electrode zone and diffuses smoothly until t=30. Later on (t=45), the MHD activity spreads the current to larger radius and reduces its value at the center. The reconnection reestablishes the current in the central zone. Finally, the profile becomes more uniform but a minimum remains near r=0.3, where the transition from open to closed flux surfaces is located. The boundary conditions applied at the flux conserver ($\mathbf{J}\times\hat{n}=0$) are responsible for the drop near r=1 and the antiparallel current observed at t=45 and t=70. Fig. 7 shows selected magnetic field lines at different times.

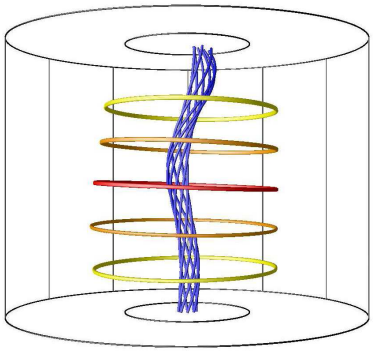

Fig. 7a. Kink, t=30

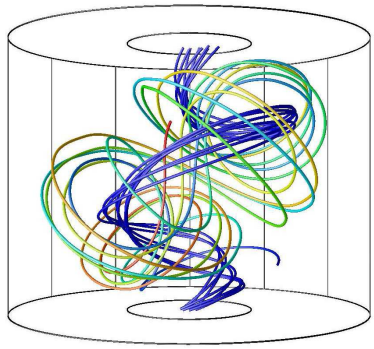

Fig. 7b. Saturation, t=45

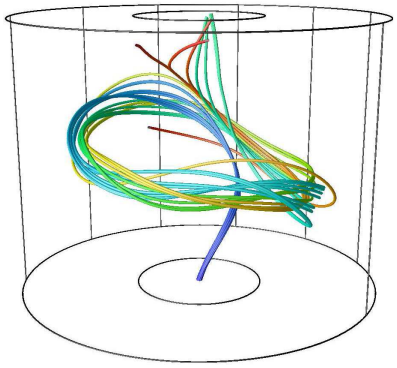

Fig. 7c. Reconnection, t=69

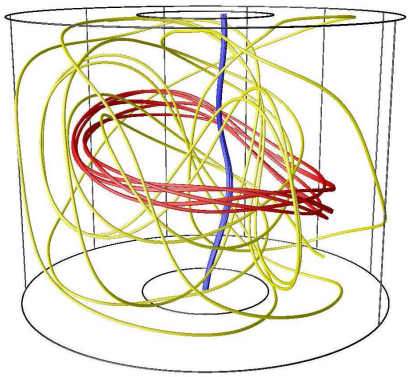

Fig. 7d. Reconnection, t=71

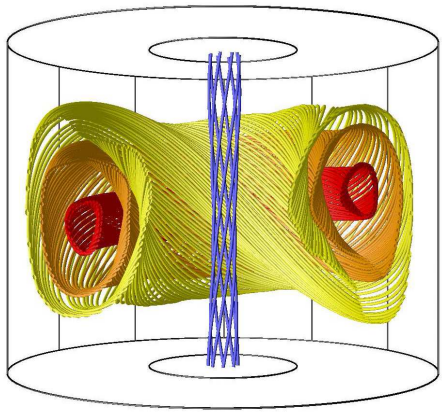

Fig. 7e. Closed flux surfaces, t=137

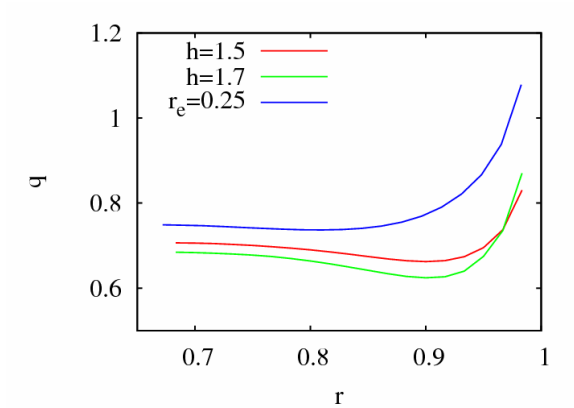

Fig.8. Safety factor profiles

Fig. 8 shows the safety factor profiles obtained for the same conditions as in Fig. 6., and also for a higher elongation (r_e=0.35, h=1.7) and a smaller elctrode radius (r_e=0.25, h=1.5).

Oscillating field current drive

Modeling Rotating Magnetic Field (RMF) current drive has been the subject of several studies. In general, an infinite plasma column is considered and the radial component of the current density is neglected. Experimental results for FRCs with RMF formation and/or sustainment generally show a higher efficiency than estimated by infinite column models. This discrepancy has been the subject of some speculation and the actual mechanism involved is not well understood, being attributed to 3D effects.

Here, we present a method to include 3D effects at the equatorial plane, where measurements are usually done. The model takes into account the radial component of Ohm's law and reproduces quite satisfactorily the observed features [8]. By considering elongated FRCs and antennae systems and properly taking into account symmetry properties of the configuration plus RMF at the equatorial plane it is possible to reduce the problem of finding steady states to the solution of two coupled nonlinear differential equations, for the real and imaginary parts of the phasor associated to the longitudinal magnetic vector potential. The boundary conditions employed correspond to matching the external RMF at the plasma-vacuum interface and requesting that the radial current density and steady poloidal magnetic stream function vanish there.

We consider a 3D FRC subject to a transverse RMF and work in the Coulomb gauge. Cylindrical coordinates r, θ, z are used and z=0 is assumed to correspond to an equatorial plane of symmetry or antisymmetry. All quantities can be expressed as the sum of a time independent part (eventually vanishing), depending only on r and z, plus a time dependent part depending on r, z and the combination θ-ωt, where ω is the frequency associated to the RMF. Some quantities are even in z while others are odd. The plasma resistivity, η, is assumed uniform and plasma density and temperature gradients are neglected.

The equations for the real and imaginary parts of the phasor of the longitudinal component of the vector potential (normalized) depend on two dimensionless parameters, λ and γ, which

are related to the classical skin depth and the applied RMF strength: $\lambda^2 = \mu_0 \omega r_s^2 / 2\eta, \gamma = b_\omega / en\eta$, where: r_s is the separatrix radius, b_ω is the normalized amplitude of the RMF and n the plasma density.

The current drive efficiency is quantified in terms of the average synchronism of the electrons. This dimensionless parameter, which is indicated with ζ, is defined as the ratio of the diamagnetism over the maximum possible or, alternatively, as the ratio of the azimuthal electron current to the current that would result if all the electrons rotate synchronously with the RMF (i.e. the average electron rotation frequency over the RMF frequency).

$$\zeta = \frac{\tilde{B}_z(1,0) - \tilde{B}_z(0,0)}{\lambda^2 / \gamma} \equiv \frac{\textit{electron average rotation frequency}}{\omega},$$

where the tilde indicates normalized quantities.

Fig. 9 presents a plot of the synchronism as a function of γ for two values of λ. The results obtained with the model presented here are indicated with dashed lines (thin line for λ=8 and thick line for λ=16) while those obtained with an infinite column model without radial current are indicated by full lines (thin for λ=8 and thick for λ=16). It can be seen that the behaviour of ζ is quite different when 3D effects and J_r are taken into account. Starting with low values of γ and low ζ the synchronism increases faster in the case with 3D effects but a larger value of γ is needed to access the region where ζ increases abruptly. On the other hand, beginning with large values of γ and ζ close to 1, where the results of both models coincide, it is possible to reduce γ further with the 3D model without entering the region where the synchronism decreases abruptly. The region with low γ and low ζ should correspond to most experimental conditions, where low penetration of the RMF is observed. The results obtained with the 3D model, which predicts higher currents in this parameter regime, show better agreement wih the experimental results than previous infinite column models.

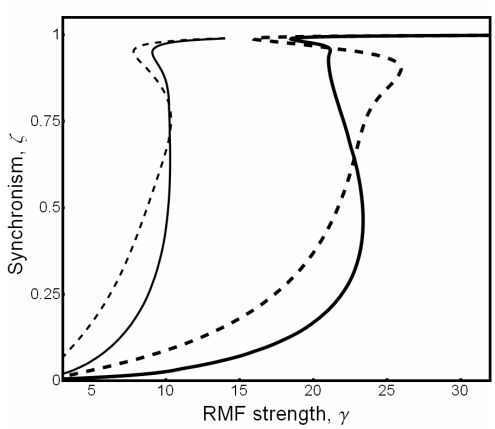

Fig. 9. Synchronism as a function of RMF strength

Fig. 1 also shows the existence of more than one synchronism value for a given λ and γ. This is a characteristic of all RMF current drive studies and is due to the nonlinear nature of the equations. We observe these features above λ=6 and a good example are the results obtained with λ=16 and no J_r (thick curve in Fig. 9), in this case there exists a small region, close to γ =21, where five different values of ζ are possible once γ is fixed.

Figs. 10 and 11 present radial profiles of the normalized azimuthal and radial current densities for λ=8, γ=7.8 and λ=16, γ=16 respectively. In both figures the low synchronism solutions are presented and the thin dotted lines show the azimuthal current density profile obtained without including 3D effects. As it can be seen, the inclusion of 3D effects results in a strong increase in the driven azimuthal current density near the axis of the plasma

column, in spite of a poor penetration of the RMF in both cases. This may be interpreted as a consequence of the existence of a region, close to the axis, where the torque arising from collisions is compensated by $J_r B_z$ and the electrons rotate essentially synchronously with the RMF. At small radii no appreciable azimuthal current density exists for the infinite column model, while at large radii the profiles practically overlap. The same overlapping occurs also for the phasors of the RMF that show very little penetration in both cases. The characteristic peaked behavior of J_r is a consequence of the nonlinear effects and the requirement that it has to vanish at the separatrix. As the synchronism and RMF penetration increase the hollow J_θ and peaked J_r profiles become less pronounced.

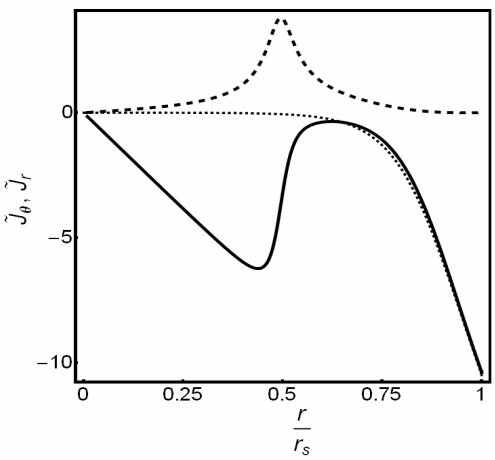

Fig. 10 Profiles of the azimuthal and radial current densities for λ=8, γ=7.8

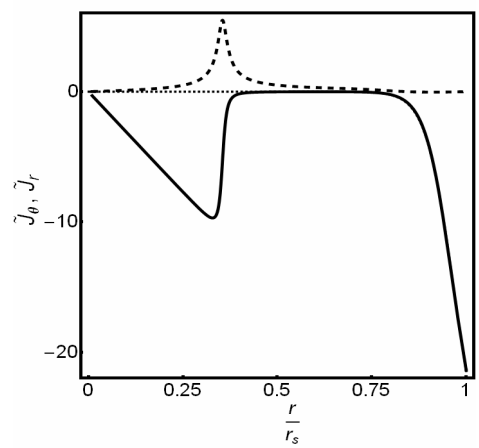

Fig. 11 Profiles of the azimuthal and radial current densities for λ=16, γ=16

[1] H. E. Ferrari y R. Farengo. *Plasma Phys. and Contr. Fusion* **49,** 713-727**,** (2007).
[2] H. E. Ferrari y R. Farengo. *Nucl. Fusion* **48**, 035014 , (2008).
[3] H. Momota et al. *Fusion Technol*. **21**, 2307 (1992).
[4] A. Lifschitz, R. Farengo and N. Arista, *Nuclear Fusion* **42**, 863-875 (2002)
[5] A. F. Lifschitz, R. Farengo y N. R. Arista, *Plasma Phys. and Contr. Fusion* **44**, 1979-1997 (2002).
[6] G. Tóth *Astrophys. Lett. Comm*. **34** 245 (1996).
[7] V. A. Izzo and T. R.Jarboe, *Phys. Plasmas***10***, 2903* (2003).
[8] R. A. Clemente, M. Gilli and R. Farengo. "Radial current density effects on rotating magnetic field current drive in field-reversed configurations". To be published in *Phys. Plasmas* (2008).